

## Shape-Controlled CO<sub>2</sub> Electrochemical Reduction on Nano-sized Pd Cubes and Octahedra

Wenlei Zhu,<sup>a,#</sup> Shyam Kattel,<sup>b,#</sup> Feng Jiao,<sup>\*,a</sup> and Jingguang G. Chen<sup>\*,b</sup>

[a] Center for Catalytic Science and Technology, Department of Chemical Engineering, University of Delaware, Newark, DE 10716 (USA)

[b] Department of Chemical Engineering, Columbia University, New York, NY 10027 (USA)

#: These authors contributed equally to this work.

Corresponding authors: jiao@udel.edu; jgchen@columbia.edu

### Abstract:

Electrochemical CO<sub>2</sub> reduction reaction (CO<sub>2</sub>RR) provides a potential pathway to mitigate challenges related to CO<sub>2</sub> emissions. Pd nanoparticles have shown interesting properties as CO<sub>2</sub>RR electrocatalysts, while how different facets of Pd affect its performance in CO<sub>2</sub> reduction to synthesis gas with controlled H<sub>2</sub> to CO ratios has not been studied. Herein, we synthesized nano-sized Pd cubes and octahedra particles dominated by Pd(100) and Pd(111) facets, respectively. The Pd octahedra particles show higher CO selectivity (up to 95%) and better activity than Pd cubes and commercial particles. For both Pd octahedra and cubes, the ratio of H<sub>2</sub>/CO products was tunable between 1 and 2, a desirable ratio for methanol production and the Fischer-Tropsch processes. Further studies of Pd octahedra in a 25-cm<sup>2</sup> flow cell showed a total CO current of 5.47 A was achieved at a potential of 3.4 V, corresponding to a CO partial current density of 220 mA/cm<sup>2</sup>. In situ X-ray absorption spectroscopy studies showed that regardless of facet Pd transformed into Pd hydride (PdH) under reaction conditions. DFT calculations show that the reduced binding energies of CO and HOCO intermediates on PdH(111) are key parameters to the high current density and Faradaic efficiency in CO<sub>2</sub> to CO conversion.

Fossil fuel utilization over the past few decades caused a rapid increase of CO<sub>2</sub> concentration in atmosphere.<sup>1,2</sup> Powered by renewable electricity, electrochemical CO<sub>2</sub> reduction reaction (CO<sub>2</sub>RR) could be a promising method to both reduce CO<sub>2</sub> emission and produce valuable chemicals.<sup>3</sup> A variety of metallic catalysts have been identified as potential candidates for electrocatalytic conversion of CO<sub>2</sub> to CO.<sup>4-9</sup> For example, Li et al. achieved CO<sub>2</sub> reduction to CO and HCOOH at low overpotentials using oxide-derived Cu films.<sup>7</sup> Zhu et al. reported CO<sub>2</sub>RR on Au nanoparticles (NPs) and found that 8 nm Au nanoparticles showed a CO Faradaic efficiency (FE) up to 90% at -0.67 V (vs reversible hydrogen electrode, RHE).<sup>9</sup> Despite the successful examples of CO selective catalysts, there are strong interests in developing an electrochemical process that can convert CO<sub>2</sub> and H<sub>2</sub>O into a synthesis gas with tunable H<sub>2</sub> to CO ratios, because the resulting synthesis gas could be directly fed into either thermochemical or biological reactors for further upgrading.<sup>10,11</sup> Therefore, research efforts are required to identify active electrocatalysts that produce synthesis gas with desirable H<sub>2</sub> to CO ratios.

Palladium (Pd) based materials have been studied as potential catalysts for electrocatalytic CO<sub>2</sub> reduction to CO and formate.<sup>12-19</sup> For example, Gao et al. reported that Pd nanoparticles with an optimal size of 3.7 nm exhibited high CO selectivity in CO<sub>2</sub>RR.<sup>16</sup> We recently showed that carbon supported Pd catalysts can simultaneously produce CO and H<sub>2</sub> in CO<sub>2</sub>RR with an adjustable H<sub>2</sub> to CO ratio between 1 and 2, which is a highly desired ratio for thermochemical synthesis of methanol and Fischer-Tropsch processes.<sup>10</sup> Due to the heterogeneous structure of the Pd/C catalysts, it was unclear regarding the preferred facets, such as Pd(111) or Pd(100), that would optimize the H<sub>2</sub>/CO ratios. By comparing the well-characterized Pd cubes and octahedra in the current study, it would allow one to directly determine the effect of crystalline facets, a key step to understand design principles for using shape-controlled Pt nanoparticles to optimize H<sub>2</sub>/CO (or CO/H<sub>2</sub>) ratios for the electrochemical reduction of CO<sub>2</sub>. Although a recent study has reported CO<sub>2</sub>RR activity over Pd(100) and Pd(111) surfaces,<sup>18</sup> Pd was considered as the active sites in that study. In the current work, the in-situ synchrotron-based X-ray absorption fine structure (EXAFS) measurements revealed the transformation of Pd to Pd-H under the CO<sub>2</sub>RR conditions. This in turn allowed us to perform DFT calculations on the Pd-H sites. The combined in-situ and DFT results identified the importance of Pd-H formation in modifying the binding energies of key intermediates, such as H, HOCO and CO, which consequently modified the activity and selectivity (CO/H<sub>2</sub> ratio) for the CO<sub>2</sub>RR.

Herein, we synthesized two different types of monodispersed Pd nanoparticles, Pd cubes and Pd octahedra with dominant Pd(100) and Pd(111) facets, respectively. The synthesis procedures for Pd nanoparticles were based on a solution method using polyvinylpyrrolidone (PVP) as a stabilizing agent and L-ascorbic acid as a reductive agent.<sup>20,21</sup> KBr was also added as a capping agent to assist the selective formation of Pd cubes.<sup>20</sup> In the case of Pd octahedra, formaldehyde was used as a mild reducing agent to grow octahedra from Pd cube seeds. By doing so, Pd atoms could deposit on the (100) facet, leading to the transformation of Pd cubes into octahedra dominated by the (111) facet.<sup>21</sup> TEM images at low magnifications (Figures 1a, c) show that Pd cubic particles have an average size of 18.4 ± 2.1 nm, whereas Pd octahedral particles have an average dimension of 29.3 ± 3.1 nm. We examined many areas of the Pd samples and concluded that both samples have a narrow size distribution (Figure S1). To check the crystal nature of Pd

particles, high resolution TEM (HRTEM) analysis was performed and the results (Figures 1b, d) show clearly lattice fringes, suggesting a high crystalline nature of both Pd samples. The distances between two neighboring fringes for the Pd cubic and octahedral particles are 0.20 and 0.22 nm, corresponding to Pd(100) and Pd(111) facets, respectively. Therefore, the Pd cubes were dominated by the Pd(100) facet, whereas the Pd octahedra were dominated by the Pd(111) facet. Powder X-ray diffraction spectra (Figure S2) also showed a preferential crystal growth along the (100) direction for the Pd cubes and the (111) direction for the Pd octahedra, which are in good agreement with the HRTEM results.

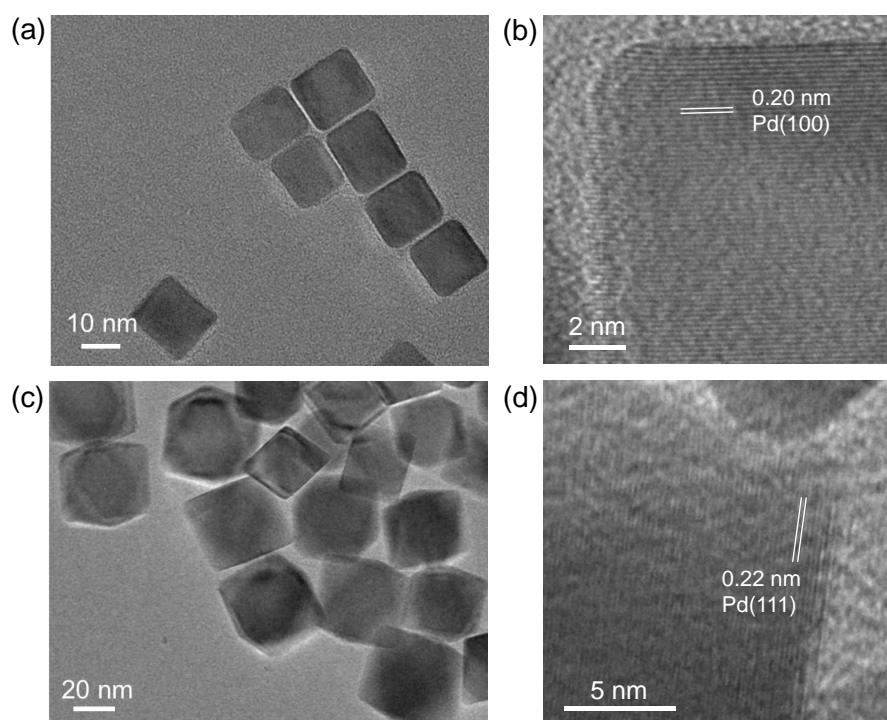


**Figure 1.** Transmission electron microscopy (TEM) images for Pd cubes and octahedra: low magnification (a, c) and high magnification (b, d), respectively.

To investigate the phase transition from Pd to PdH in both cubes and octahedra during the CO<sub>2</sub>RR, we performed in situ X-ray absorption spectroscopic (XAS) measurements in a CO<sub>2</sub>-saturated 0.5 M NaHCO<sub>3</sub> electrolyte. The Pd K-edge X-ray absorption near-edge spectroscopy (XANES) results at various applied potentials are shown in Figures 2. Increasing the overpotential resulted in a clear shift of both peaks to lower energy, suggesting the formation of PdH.<sup>10,22</sup> Peak A showed dipole allowed transition from Pd 1s to the 4d5p hybridized unoccupied states, and Peak B corresponded to the transition from Pd 1s to 4f state.<sup>23,24</sup> The energy shift of Peak A was attributed to the mix of Pd anti-bonding bands with the unoccupied s and p orbitals of absorbed H atoms.<sup>25,26</sup> The Pd K-edge extended X-ray absorption fine structure (EXAFS) spectra are fitted to illustrate the Pd structural change during the CO<sub>2</sub>RR (Figures S3, S4). The Pd–Pd bond length remains unchanged above -0.4 V at 2.731 Å. When the potential decreases to below -0.4 V, Pd-Pd bond length gradually increased to ~2.740 Å and then quickly increased to ~2.830 Å for both cubic and octahedral particles, indicating the formation of PdH at approximately -0.5 V. The phase transition from Pd to PdH clearly caused a lattice expansion in the Pd-based catalysts. Based on existing literature, underpotential

deposition of H on Pd could occur at potentials around 0V (vs. RHE).<sup>12</sup> However, our XAS results reveal that well-defined PdH phase is not formed until a potential of lower than -0.5 (vs. RHE), suggesting the presence of surface hydrogen and/or amorphous PdH in the potential range between 0 and -0.5 V (vs. RHE).. On Pd(111), our DFT calculations show that H adsorption on the surface is thermodynamically more favorable by 0.33 eV compared to subsurface H adsorption. Furthermore, previous DFT calculations have shown that the energy barrier for H migration from surface to subsurface on Pd(111) is  $\sim 0.4$  eV.<sup>27</sup> This suggests that surface H could potentially migrate to the subsurface and form bulk PdH phase at high negative potential in agreement with the experimental observations.

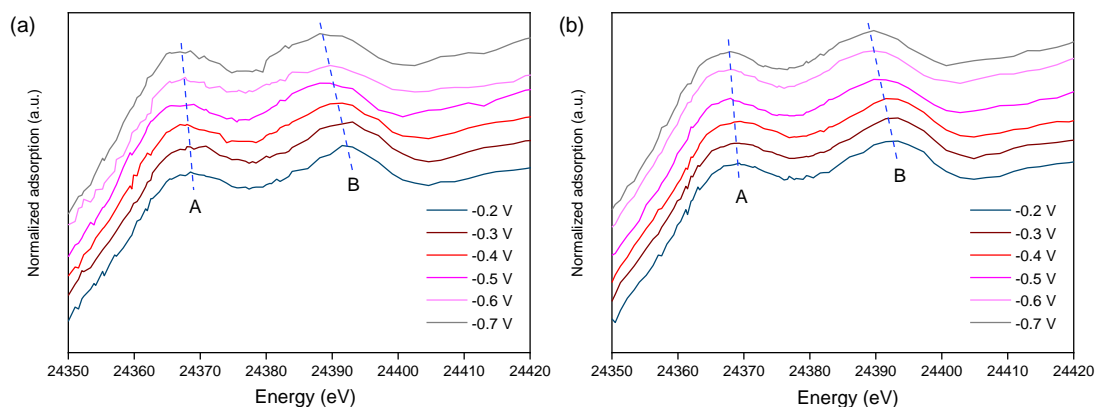


**Figure 2.** In situ structural characterization of Pd/C catalyst under the CO<sub>2</sub>RR conditions using X-ray absorption spectroscopy. In situ XANES spectra of Pd K-edge for (a) Pd octahedra and (b) Pd cubes.

The electrocatalytic properties of Pd particles were first evaluated in a two-compartment three-electrode batch cell. A commercial Pd nanoparticle sample was also studied for comparison (structural characterization data is shown in Figures S2, S5). The electrodes were made by drop-casting a solution containing a certain concentration of Pd nanoparticles, isopropanol and Nafion on gas diffusion layer (GDL). The CO<sub>2</sub> electrolysis experiments were performed in a CO<sub>2</sub>-saturated high purity 0.5M sodium bicarbonate (NaHCO<sub>3</sub>) electrolyte under ambient conditions. The gas products were analyzed using a gas chromatography and the liquid products were measured by <sup>1</sup>H nuclear magnetic resonance spectroscopy. Figure 3a shows both CO and H<sub>2</sub> Faradaic efficiencies under a variety of applied potentials. Among all the three Pd catalysts, the Pd octahedra catalyst exhibited the highest CO selectivity of 94% at an applied voltage of -0.7 V vs. reversible hydrogen electrode (RHE, all the voltages are on the RHE scale unless stated otherwise), which is comparable to current state-of-the-art Pd catalysts reported in the literature (Table S1). At potentials more negative than -0.7 V, CO Faradaic efficiency decreased significantly and H<sub>2</sub> production increased substantially, which could be caused by the mass transport of CO<sub>2</sub> to active sites. At very negative potentials, H<sub>2</sub> and CO were the dominant products for all Pd catalysts, while a significant amount of formate was detected at potentials high than -0.5 V (Figure S6), which can be attributed to the active phase switched from Pd to  $\beta$ -PdH at relatively negative potentials.<sup>12</sup> More detailed studies on the presence of different PdH phases at different potential regions have been reported by Gao et al.<sup>12</sup> A relative low current density was observed for commercial Pd/C catalyst, which was likely due to the strong CO adsorption on edge and corner sites in the sample.

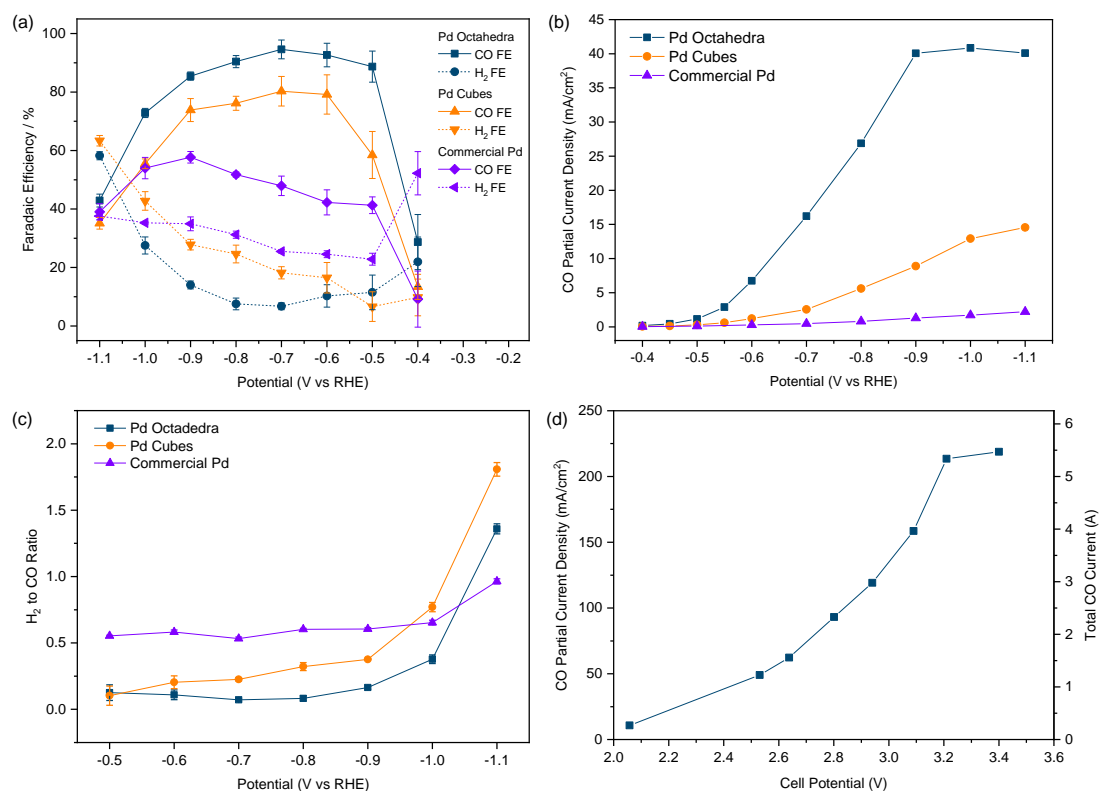


**Figure 3.** Electrocatalytic CO<sub>2</sub> reduction results for Pd octahedra and cubes in a batch cell: (a) Faradaic efficiencies, (b) CO partial current densities (normalized to electrode areas), and (c) H<sub>2</sub> to CO ratios. Results for commercial Pd were also shown for comparison. Flow cell test results for Pd octahedra catalyst were shown in (d). All the batch experiments were performed in CO<sub>2</sub>-saturated 0.5M NaHCO<sub>3</sub> electrolytes (pH = 7.2).

CO partial current densities at various potentials are showed in Figure 3b (current density profiles can be found in Figure S7), where Pd octahedra exhibited a much higher CO partial current density ( $\sim 41$  mA/cm<sup>2</sup> at -0.9 V) than that of Pd cubes ( $\sim 15$  mA/cm<sup>2</sup>). We also calculated current densities based on the estimated Pd surface areas using their loadings and sizes (Figure S8 and Table S2). The Pd octahedra exhibited a more than 3 times higher CO partial current density than Pd cubes, suggesting that the Pd(111) surface is more active than the Pd(100) surface in CO<sub>2</sub>RR. The plateau of maximum CO partial current density for the Pd octahedra was caused by CO<sub>2</sub> transport issues due to the low CO<sub>2</sub> solubility in aqueous bicarbonate electrolyte.<sup>8</sup> In comparison to Pd cubes and octahedra, the commercial Pd catalyst showed a much lower CO Faradaic efficiency (<60%) and an extremely low current density (<3 mA/cm<sup>2</sup>) under test conditions. We suspect that it may be due to the fact that the commercial Pd particles have a rough surface populated with low coordinated sites that unfavorably bind to intermediates for CO formation. The H<sub>2</sub> to CO products ratio for Pd cubes and octahedra at different applied potentials are shown in Figure 3c. At relatively negative potentials (i.e., high current densities), the H<sub>2</sub> to CO ratios for both Pd cubes and octahedra fall into the desired ratios of synthesis gas for Fischer-Tropsch process and methanol synthesis. The stability of Pd octahedra and cubes was examined using TEM and the results (Figure S8) showed no obvious morphology change to the catalysts.

The transport limitation of CO<sub>2</sub> in the batch cell could be circumvented by using a flow cell system, where gaseous CO<sub>2</sub> is fed directly to the catalyst surface.<sup>28-30</sup> Because Pd octahedral catalyst exhibited the best performance in the batch cell tests, we chose it for the flow cell investigation. Pd octahedral particles were first sprayed onto a 25 cm<sup>2</sup> gas-diffusion layer (i.e., a porous carbon support) with a Pd loading of 0.3 mg/cm<sup>2</sup>, which served as the cathode. IrO<sub>2</sub> (loading: 1 mg/cm<sup>2</sup>) was used as the anode and 1M KOH was used as the anolyte. A schematic diagram of the whole flow cell setup is shown in Figure S9. Remarkably, a CO partial current densities up to 220 mA/cm<sup>2</sup> (corresponding to a total CO current of 5.5 A) together with a CO Faradaic efficiency of ~92% was achieved at a cell potential of 3.2 V (Figure S10).

**Table1:** DFT calculated binding energies (in eV) of H, CO and HOCO on Pd and PdH surfaces.

| Species | Pd(111) | Pd(100) | PdH(111) | PdH(100) |
|---------|---------|---------|----------|----------|
| H       | -0.58   | -0.49   | 0.12     | -0.10    |
| CO      | -2.03   | -1.96   | -0.50    | -1.29    |
| HOCO    | -2.21   | -2.50   | -1.73    | -2.16    |

DFT calculations were performed to gain further insights into the CO selectivity of Pd(111) and Pd(100) surfaces. Table 1 summarizes the DFT calculated binding energies (optimized configurations are shown in Figure S11) of reaction intermediates involved in CO<sub>2</sub>RR and HER on Pd/PdH(111) and Pd/PdH(100) surfaces. The binding energies of \*H and \*CO are similar on both Pd(111) and Pd(100). \*CO binds strongly on Pd(111) and Pd(100), thus its desorption is predicted to be difficult at electrochemical conditions. In contrast, all intermediates bind much more strongly on PdH(100) compared to PdH(111). The change in Gibbs free energy ( $\Delta G$ ) for CO<sub>2</sub>RR along the carboxyl (\*HOCO) and formate (\*HCOO) pathways and HER at a potential (U) = 0 V were calculated (see Computational Methods for details) and presented in Figure 4 and Figure S12. As shown in Figure 4a, the HER activity of Pd(111) and Pd(100) is limited by \*H desorption whereas \*H adsorption is the limiting step on the PdH(111) and PdH(100) surfaces. Thus the HER is predicted to be downhill in energy at applied negative potential of U = -0.34 V and U = -0.12 V on PdH(111) and PdH(100), respectively. It is found that the CO<sub>2</sub>RR via the \*HOCO pathway is energetically more favorable over \*HCOO pathway on Pd(111), Pd(100) and PdH(111), while the \*HCOO pathway is slightly favorable over \*HOCO pathway on PdH(100) (Figure S12). Figure 4b shows that \*HOCO/\*HCOO is stabilized on Pd(111) and Pd(100). However, \*CO is strongly bound, which makes \*CO desorption uphill in energy by 1.51 eV and 1.44 eV on Pd(111) and Pd(100), respectively. Thus \*CO desorption is the rate limiting step on both Pd(111) and Pd(100) surfaces. In comparison, on PdH(100), Figure 4b shows that \*CO desorption is the most difficult step and is uphill in energy by 0.77 eV. In contrast, it is noted that \*CO desorption is thermoneutral on PdH(111) and no longer a rate limiting step. As a result, \*CO desorption is much more facile on PdH(111) compared to PdH(100). Therefore, the DFT results are in agreement with the experimental findings of higher CO selectivity on PdH(111) (Pd octahedra) than PdH(100) (Pd cubes) due to the facile desorption of \*CO from the PdH(111) surface.

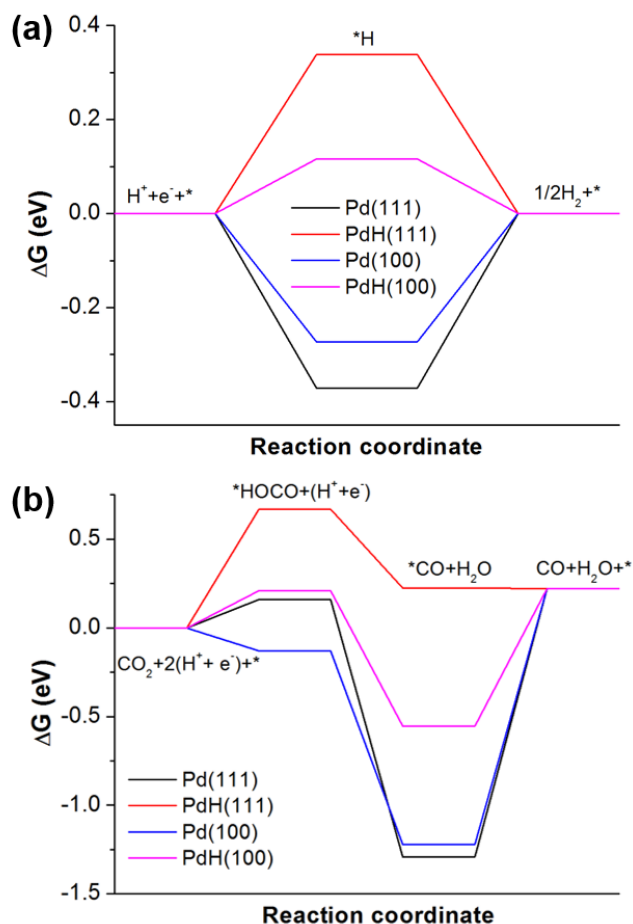


**Figure 4.** DFT calculated free energy diagrams: (a) HER and (b) CO<sub>2</sub>RR on Pd(111), Pd(100), PdH(111) and PdH(100).

In summary, we showed that both Pd cubic and octahedral nanoparticles have been successfully synthesized and investigated as potential electrocatalysts for CO<sub>2</sub>RR. The PdH(111) surface of Pd octahedra exhibited higher CO Faradaic efficiency and CO partial current density than the Pd(100) surface in Pd cubes. In situ XAS studies confirmed the phase transition from Pd to PdH at about -0.5 V. DFT calculations unravel the origin of high CO selectivity and activity to the weaker CO binding energy on PdH. Therefore, tuning the relative adsorption strength of CO, HOCO and H on nanoparticles with controlled morphology could offer opportunities to increase synthesis gas production rate and tune H<sub>2</sub> to CO products ratio.

## Methods

### *Synthesis and characterization of Pd nanoparticles*

Pd cubic nanoparticles were synthesized according to a previously published method.<sup>20</sup> Typically, 8.0 mL of an aqueous solution containing KBr (600 mg), PVP (105 mg) and L-ascorbic acid (60 mg) was added into an 11 drum Vial. This vial was heated in air under magnetic stirring at 80 °C in an oil bath for 10 min. Subsequently, 3.0 mL of an aqueous solution of Na<sub>2</sub>PdCl<sub>4</sub> (57 mg) was added with a pipette. After the vial had been loosely capped, the reaction could proceed at 80 °C in an oil bath for 3 h. The products

were collected by centrifuging in water for 3 times (10000 RPM, 10 min). Precipitates were redispersed in 11 mL water.

Pd octahedral nanoparticles were synthesized according to literature.<sup>21</sup> Typically, 3.0 mL of an aqueous solution containing 14.5 mg of Na<sub>2</sub>PdCl<sub>4</sub> was introduced into 7.7 mL of a mixture containing AA (60 mg), PVP (105 mg), KBr (300 mg), and 0.3 mL of the 18 nm Pd seeds, which had been heated at 60 °C for 5 min under magnetic stirring. The product was collected by centrifugation, washed ten times (10000 RPM, 10 min) with water to remove surfactant, and redispersed in ethanol for further process.

The as-synthesized Pd catalysts were characterized using TEM (JEOL JEM-3010) and powder XRD (Bruker D8). In situ X-ray absorption spectroscopy (XAS) measurements were performed at the 5-BM-D beamline at Argonne National Laboratory.

#### *Electrochemical CO<sub>2</sub> reduction test*

A Princeton Applied Research VersaSTAT 3 potentiostat was used for all CO<sub>2</sub> reduction experiments. A carbon rod was used as the counter electrode. The electrolyte was 0.5M NaHCO<sub>3</sub> saturated with CO<sub>2</sub> with pH of 7.2. All potentials were measured against an Ag/AgCl reference electrode (3.0M KCl, BASi), iR corrected and converted to RHE. Electrolysis was performed under room temperature in a gas-tight two-compartment electrochemical cell with two halves separated and connected with a piece of Nafion<sup>®</sup> 117 membrane. Before each experiment, the electrolyte was purged again with CO<sub>2</sub> gas for at least 30 min and the headspace for at least 20 min. Gas products were analyzed every 30 min using a gas chromatograph (SHIMADZU, GC-2014) equipped with PLOT MolSieve 5A and Q-bond PLOT columns, whereas liquid products were analyzed on a Bruker AVIII 600MHz NMR spectrometer. Faradaic efficiency calculation was based on methods described in previous papers.<sup>9,10</sup>

For the flow cell tests, the experiments were performed in a two-channel flow cell with channels of dimension 5×5×0.15 cm<sup>3</sup>. The gas flow rate into the flow cell was controlled at 100 sccm via a Brooks GF40 mass flow controller. The anolyte flow rates were controlled via a peristaltic pump at 10 mL/min. The cathode and anode were separated via a Sustainion<sup>®</sup> anion exchange membrane.

#### **References:**

- (1) Malhi, Y.; Meir, P.; Brown, S. Forests, carbon and global climate. *Philosophical Transactions of the Royal Society of London. Series A: Mathematical, Physical and Engineering Sciences* **2002**, *360*, 1567-1591.
- (2) Gillett, N. P.; Arora, V. K.; Zickfeld, K.; Marshall, S. J.; Merryfield, W. J. Ongoing climate change following a complete cessation of carbon dioxide emissions. *Nat. Geosci.* **2011**, *4*, 83.
- (3) Lu, Q.; Jiao, F. Electrochemical CO<sub>2</sub> reduction: Electrocatalyst, reaction mechanism, and process engineering. *Nano Energy* **2016**, *29*, 439-456.
- (4) Yoshio, H.; Katsuhei, K.; Shin, S. PRODUCTION OF CO AND CH<sub>4</sub> IN

- ELECTROCHEMICAL REDUCTION OF CO<sub>2</sub> AT METAL ELECTRODES IN AQUEOUS HYDROGENCARBONATE SOLUTION. *Chem. Lett.* **1985**, *14*, 1695-1698.
- (5) Hori, Y.: Electrochemical CO<sub>2</sub> Reduction on Metal Electrodes. In *Modern Aspects of Electrochemistry*; Vayenas, C. G., White, R. E., Gamboa-Aldeco, M. E., Eds.; Springer New York: New York, NY, 2008; pp 89-189.
- (6) Hansen, H. A.; Shi, C.; Lausche, A. C.; Peterson, A. A.; Norskov, J. K. Bifunctional alloys for the electroreduction of CO<sub>2</sub> and CO. *PCCP* **2016**, *18*, 9194-9201.
- (7) Li, C. W.; Kanan, M. W. CO<sub>2</sub> Reduction at Low Overpotential on Cu Electrodes Resulting from the Reduction of Thick Cu<sub>2</sub>O Films. *J. Am. Chem. Soc.* **2012**, *134*, 7231-7234.
- (8) Lu, Q.; Rosen, J.; Zhou, Y.; Hutchings, G. S.; Kimmel, Y. C.; Chen, J. G.; Jiao, F. A selective and efficient electrocatalyst for carbon dioxide reduction. *Nat. Commun.* **2014**, *5*, 3242.
- (9) Zhu, W.; Michalsky, R.; Metin, Ö.; Lv, H.; Guo, S.; Wright, C. J.; Sun, X.; Peterson, A. A.; Sun, S. Monodisperse Au Nanoparticles for Selective Electrocatalytic Reduction of CO<sub>2</sub> to CO. *J. Am. Chem. Soc.* **2013**, *135*, 16833-16836.
- (10) Sheng, W.; Kattel, S.; Yao, S.; Yan, B.; Liang, Z.; Hawxhurst, C. J.; Wu, Q.; Chen, J. G. Electrochemical reduction of CO<sub>2</sub> to synthesis gas with controlled CO/H<sub>2</sub> ratios. *Energy Environ. Sci.* **2017**, *10*, 1180-1185.
- (11) Haas, T.; Krause, R.; Weber, R.; Demler, M.; Schmid, G. Technical photosynthesis involving CO<sub>2</sub> electrolysis and fermentation. *Nat. Catal.* **2018**, *1*, 32-39.
- (12) Gao, D. F.; Zhou, H.; Cai, F.; Wang, D. N.; Hu, Y. F.; Jiang, B.; Cai, W. B.; Chen, X. Q.; Si, R.; Yang, F.; Miao, S.; Wang, J. G.; Wang, G. X.; Bao, X. H. Switchable CO<sub>2</sub> electroreduction via engineering active phases of Pd nanoparticles. *Nano Research* **2017**, *10*, 2181-2191.
- (13) Gao, D. F.; Zhou, H.; Cai, F.; Wang, J. G.; Wang, G. X.; Bao, X. H. Pd-Containing Nanostructures for Electrochemical CO<sub>2</sub> Reduction Reaction. *ACS Catal.* **2018**, *8*, 1510-1519.
- (14) Jiang, B.; Zhang, X. G.; Jiang, K.; Wu, D. Y.; Cai, W. B. Boosting Formate Production in Electrocatalytic CO<sub>2</sub> Reduction over Wide Potential Window on Pd Surfaces. *J. Am. Chem. Soc.* **2018**, *140*, 2880-2889.
- (15) Klinkova, A.; De Luna, P.; Dinh, C. T.; Voznyy, O.; Larin, E. M.; Kumacheva, E.; Sargent, E. H. Rational Design of Efficient Palladium Catalysts for Electroreduction of Carbon Dioxide to Formate. *ACS Catal.* **2016**, *6*, 8115-8120.
- (16) Gao, D.; Zhou, H.; Wang, J.; Miao, S.; Yang, F.; Wang, G.; Wang, J.; Bao, X. Size-Dependent Electrocatalytic Reduction of CO<sub>2</sub> over Pd Nanoparticles. *J. Am. Chem. Soc.* **2015**, *137*, 4288-4291.
- (17) Huang, H.; Jia, H.; Liu, Z.; Gao, P.; Zhao, J.; Luo, Z.; Yang, J.; Zeng, J. Understanding of Strain Effects in the Electrochemical Reduction of CO<sub>2</sub>: Using Pd Nanostructures as an Ideal Platform. *Angew. Chem. Int. Ed.* **2017**, *56*, 3594-

- 3598.
- (18) Dong, H.; Zhang, L.; Yang, P.; Chang, X.; Zhu, W.; Ren, X.; Zhao, Z.-J.; Gong, J. Facet design promotes electroreduction of carbon dioxide to carbon monoxide on palladium nanocrystals. *Chem. Eng. Sci.* **2018**.
  - (19) Zhuang, T.-T.; Liang, Z.-Q.; Seifitokaldani, A.; Li, Y.; De Luna, P.; Burdyny, T.; Che, F.; Meng, F.; Min, Y.; Quintero-Bermudez, R.; Dinh, C. T.; Pang, Y.; Zhong, M.; Zhang, B.; Li, J.; Chen, P.-N.; Zheng, X.-L.; Liang, H.; Ge, W.-N.; Ye, B.-J.; Sinton, D.; Yu, S.-H.; Sargent, E. H. Steering post-C–C coupling selectivity enables high efficiency electroreduction of carbon dioxide to multi-carbon alcohols. *Nat. Catal.* **2018**, *1*, 421-428.
  - (20) Jin, M.; Liu, H.; Zhang, H.; Xie, Z.; Liu, J.; Xia, Y. Synthesis of Pd nanocrystals enclosed by {100} facets and with sizes <10 nm for application in CO oxidation. *Nano Research* **2011**, *4*, 83-91.
  - (21) Jin, M.; Zhang, H.; Xie, Z.; Xia, Y. Palladium nanocrystals enclosed by {100} and {111} facets in controlled proportions and their catalytic activities for formic acid oxidation. *Energy Environ. Sci.* **2012**, *5*, 6352-6357.
  - (22) Bugaev, A. L.; Guda, A. A.; Lomachenko, K. A.; Srabionyan, V. V.; Bugaev, L. A.; Soldatov, A. V.; Lamberti, C.; Dmitriev, V. P.; van Bokhoven, J. A. Temperature- and Pressure-Dependent Hydrogen Concentration in Supported PdHx Nanoparticles by Pd K-Edge X-ray Absorption Spectroscopy. *J. Phys. Chem. C* **2014**, *118*, 10416-10423.
  - (23) Lin, C.-M.; Hung, T.-L.; Huang, Y.-H.; Wu, K.-T.; Tang, M.-T.; Lee, C.-H.; Chen, C. T.; Chen, Y. Y. Size-dependent lattice structure of palladium studied by x-ray absorption spectroscopy. *Phys. Rev. B* **2007**, *75*, 125426.
  - (24) Muller, J. E.; Jepsen, O.; Andersen, O. K.; Wilkins, J. W. Systematic Structure in the K-Edge Photoabsorption Spectra of the 4d Transition Metals: Theory. *Phys. Rev. Lett.* **1978**, *40*, 720-722.
  - (25) Sham, T. K. L-edge x-ray-absorption systematics of the noble metals Rh, Pd, and Ag and the main-group metals In and Sn: A study of the unoccupied density of states in 4d elements. *Phys. Rev. B* **1985**, *31*, 1888-1902.
  - (26) Müller, J. E.; Wilkins, J. W. Band-structure approach to the x-ray spectra of metals. *Phys. Rev. B* **1984**, *29*, 4331-4348.
  - (27) Greeley, J.; Mavrikakis, M. Surface and subsurface hydrogen: Adsorption properties on transition metals and near-surface alloys. *J Phys Chem B* **2005**, *109*, 3460-3471.
  - (28) Jouny, M.; Luc, W.; Jiao, F. *Nat. Catal.* **2018**, *1*, 748-755.
  - (29) Jhong, H. R.; Ma, S. C.; Kenis, P. J. A. Electrochemical conversion of CO<sub>2</sub> to useful chemicals: current status, remaining challenges, and future opportunities. *Curr. Opin. Chem. Eng.* **2013**, *2*, 191-199.
  - (30) Dinh, C. T.; Burdyny, T.; Kibria, M. G.; Seifitokaldani, A.; Gabardo, C. M.; de Arquer, F. P. G.; Kiani, A.; Edwards, J. P.; De Luna, P.; Bushuyev, O. S.; Zou, C. Q.; Quintero-Bermudez, R.; Pang, Y. J.; Sinton, D.; Sargent, E. H. CO<sub>2</sub> electroreduction to ethylene via hydroxide-mediated copper catalysis at an abrupt interface. *Science* **2018**, *360*, 783-787.

**Acknowledgements:**

Authors from Columbia University are partially supported by the US Department of Energy, Catalysis Program (DE-FG02-13ER16381). Authors at University of Delaware thank the financial support from the Department of Energy under Award Number DE-FE0029868. The authors also thank the National Science Foundation Faculty Early Career Development program (Award No. CBET-1350911). This research used resources of the Advanced Photon Source, a U.S. Department of Energy (DOE) Office of Science User Facility operated for the DOE Office of Science by Argonne National Laboratory under Contract No. DE-AC02-06CH11357. The DFT calculations were performed using computational resources at the Center for Functional Nanomaterials, a user facility at Brookhaven National Laboratory.